JOURNAL OF THERMOPHYSICS AND HEAT TRANSFER
Vol. 23, No. 3, July–September 2009

Simulation of Carbon–Carbon Crack Growth Due to Carbon Oxidation at High Temperatures

Evgeni Titov,* Jiaqiang Zhong,† and Deborah A. Levin‡
Pennsylvania State University, University Park, Pennsylvania 16802
and
Donald J. Picetti§
The Boeing Company, Huntington Beach, California 92647

DOI: 10.2514/1.39060

High-temperature gas-dynamic computational techniques are employed to study microflows in expanding crack channels caused by the oxidation of the channel carbon walls. Wall regression rates for three reinforced carbon–carbon samples that were tested in a high-enthalpy arcjet environment were modeled. The test geometries and flow conditions span flow regimes from the transitional through the continuum, but the same mechanism for wall material loss, atomic oxygen reaction with bare carbon, was used in all three cases. Kinetic (direct simulation Monte Carlo) and continuum (Navier–Stokes) gas-dynamic approaches were used. The predicted wall regression rates were found to agree with arcjet measurements, and the general specimen shape change was predicted. Local gas flowfield results were found to affect the oxidation rate in a manner that cannot be predicted by previous mass loss correlations. The method holds promise for future modeling of materials gas-dynamic interactions for hypersonic flight.

I. Introduction

DUE to its brittle nature, the reinforced carbon–carbon (RCC) wing leading edge and nose cap region of the space shuttle are vulnerable to cracks that may be formed through micrometeoroid and orbital debris impact [1]. Once cracks are formed, the freestream species, including reactive atomic O, may penetrate through the bare carbon-crack channel and oxidize the channel wall, leading to a growth mechanism of the crack that can pose severe material damage. The crack expansion process in RCC samples has been observed in ground-based arcjet tests performed at NASA Johnson Space Center and has certainly been a continuing concern for operational shuttle flights. To facilitate the thermal protection system (TPS) design of the space shuttle, and future vehicles, it is important to understand the carbon oxidation crack-channel growth mechanism during the shuttle reentry process. The present procedures for determining whether a damage site will increase in size to a dangerous level is performed efficiently with mass correlation relationships typically based on freestream conditions [2]. However, these mass correlations, although useful, are based on arcjet testing for specific geometries and conditions and therefore cannot take into account local gas-dynamic conditions.

As one considers the development of fundamental models to determine damaged site growth for exposed carbon fiber materials, a second challenge arises. The question of how to couple the small-scale damage site on the shuttle RCC vehicle surface to the vehicle flowfield becomes important. This coupling can give rise to a wide range of flowfields, from local flow disturbances that can safely be decoupled from the larger vehicle flowfield [3] to cases in which the flow inside the damaged region can influence the shock wave structure in front of it [4]. The operational goal is to develop a tool that can predict whether the damage site will increase during reentry to the point of causing a critical breach of the TPS system. As a precursor to that endpoint, it is first necessary to propose and validate an RCC damage model against ground-based arcjet tests.

The purpose of this work is to demonstrate a physical model that may be employed in numerical simulations of microflows through a carbon channel shaped crack and to predict crack propagation processes for ground-based arcjet testing. The modeling and simulation of crack growth rates and shape changes for the three arcjet RCC tests that were considered are summarized in Fig. 1 and Tables 1 and 2. The images on the left- and right-hand sides of Fig. 1 show the damaged RCC samples before and after arcjet testing. The second and third rows show the front and backside surfaces of the 1151 hypervelocity impact tests [5]. The three cases were chosen to cover different flow conditions and dimensionality, with the 1151 hypervelocity impact tests [5] providing the most instrumentation. The general idea of the three tests is similar. A well-characterized damage shape is created by removal of the silicon carbide protective layer of the RCC to expose the bare carbon matrix fibers.

We wish to accurately predict the growth of a damage site on a space vehicle by taking into account local gas-dynamic effects, but in a computationally tractable manner. This requires the accurate modeling of the high-temperature, hypersonic gases and the expanding crack wall. Depending on the dimensions of the crack and the degree of rarefaction of the gas environment (particularly for low Earth orbit), the flow modeling through the channel crack may require different flowfield computational techniques. For example, for the first case considered, 1904, the Knudsen number, defined as the ratio of the mean free path to the minimum crack-channel dimension, is in the range of 0.02–0.5, suggesting that the initial crack flow is in the transition regime where velocity slip and temperature jump close to the wall exists. The Knudsen numbers for cases 1151 and 2033, however, are much lower. Therefore, in this work, the flow gas dynamics were modeled using different flowfield modeling techniques, including direct simulation Monte Carlo (DSMC), a collision-limiting version known as equilibrium direct simulation Monte Carlo (eDSMC) [6], and Navier–Stokes (NS). Table 1 summarizes the flowfield models used for the three cases. For all three flowfield models, the same physical mechanism for carbon wall consumption will be employed. Atomic oxygen impacting a bare carbon wall is assumed to chemically react with the wall to produce CO gas that then enters the flowfield. The probability of the reaction

Presented as Paper 4469 at the 18th AIAA Computational Fluid Dynamics Conference, Miami, Florida, 25–28 June 2007; received 11 June 2008; revision received 25 October 2008; accepted for publication 28 December 2008.

*Postdoctoral Research Fellow, Department of Aerospace Engineering.
†Postdoctoral Research Fellow, Department of Aerospace Engineering.
‡Professor, Department of Aerospace Engineering. Associate Fellow AIAA.
§Associate Technical Fellow, Flight Sciences and Advanced Design. Member AIAA.

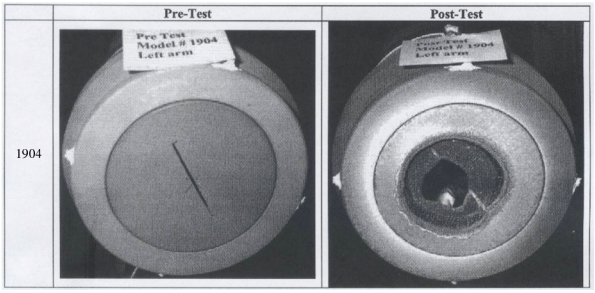

a) Case 1904

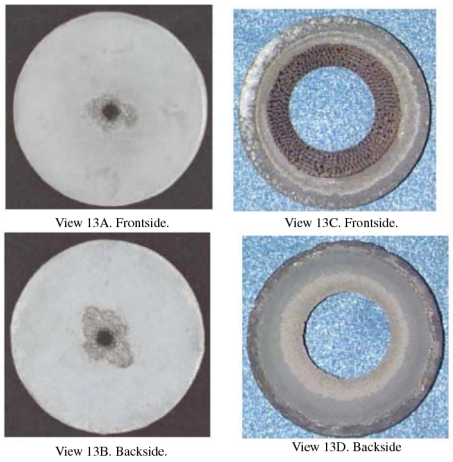

b) Case 1151

c) Case 2033

Fig. 1 Summary of the three arcjet cases studied in this work.

is the only free parameter in the model, with a value of 0.9 used in all simulations [7].

The modeling of flow through channels has been an active area of microfluidic research for both DSMC and NS methods. The work of Liou and Fang [8], Alexeenko et al. [9], and Sun and Faghri [10] are a few of the many papers that have discussed the use of DSMC in channel flow modeling. Liou and Fang [8] studied the heat transfer characteristics of supersonic flows in microchannels for Knudsen numbers ranging from 0.031 to 0.186. In the work of Alexeenko et al. [9], analytic expressions were obtained for pressure drop and mass flux in pressure-driven constricted microchannels and compared with DSMC calculations. Finally, Sun and Faghri [10] studied the impact of wall roughness on the microchannel flows. Navier–Stokes solutions with no-slip and slip correction have also been successfully employed to model flow through channels in the appropriate Knudsen number regime [11].

The paper is organized as follows. The interactions between gas molecules and the crack channel are briefly discussed in Sec. II, along with a brief description of the three flowfield computational methods employed. In Sec. III, the geometry of the three cases is presented and discussed. For the 1904 case, two- and three-dimensional DSMC approaches are employed to test the sensitivity of the wall regression rate to the dimensionality of the flow. For the 1151 case the problem is axisymmetric, and for the 2033 wedge case the flow is fully three-dimensional, but a 2-D approximation for the 2033 wedge case is also considered. Finally, in Sec. IV, we present the flowfield and wall regression rates, as well as the wall shape changes, in a comparison with the arcjet data. The effect of wall chemistry on the flow external to the channel as well as the internal channel flow is considered. We analyze the degree of change in the flowfield as the crack channel deforms for the different cases. In Sec. V, we summarize our conclusions and suggest future research directions.

II. Numerical Methods

A. Wall Oxidation Model

An important feature of the crack flow modeling is the interactions between the gas species and the channel wall rather than chemical reactions in the gaseous flow. In preliminary calculations, we found that the chemical reactions among gas species (such as $O+N_2 \rightarrow NO+N$) are rare in the channel flow because the total reaction energy of the colliding molecules for a gas temperature of 4000 K is usually less than the chemical activation energy. Also it was found that the flow residence time in the channel was too short for chemical reactions to occur. For these reasons, the flows discussed in this work do not include gas species chemical reactions.

An important distinction between arcjet and furnace materials testing is that, in the former, there is a high fraction of atomic oxygen and a negligible amount of molecular oxygen present. Both atomic as well as molecular oxygen will react with a bare carbon wall, but the reaction probability of atomic oxygen is higher with almost no activation energy required. As discussed in [12], atomic O plays an important role in carbon mass surface loss. Rosner and Allendorf [7] give a reaction probability close to 0.9 for the gas-surface reaction

$$C_{(s)} + O \rightarrow CO \tag{1}$$

where the gaseous atomic O temperature is about 1500 K, $C_{(s)}$ is a carbon atom at the wall surface, and the other species are gaseous. We can estimate the mass loss due this gas-surface reaction in a simple calculation. As the gas travels through the channel, it collides with the carbon wall with a number flux normal to the channel wall, $\dot{N}$, given as [13]

$$\dot{N} = n_O/(2\sqrt{\pi}\beta) \tag{2}$$

where n_O is the atomic O number density, and β is the reciprocal of the molecular most probable thermal velocity. The mass loss, surface regression rate, $\dot{S}$, is related to $\dot{N}$ by

$$\dot{S} = (\dot{N}/n_C)P \tag{3}$$

where n_C is the carbon number density (a mass density value of 1.575 gm/cm^3 was assumed), and P is the reaction probability for the $C_{(s)} + O$ reaction. Using typical values in the boundary-layer region of the channel flowfield of $n_O = 3.0 \times 10^{21}$ m^{-3}, $T=$ 2400 K, and a reaction probability of 0.9, we obtain an approximate surface regression rate of 0.02 mm/s. This wall regression rate will be shown in Sec. IV to be typical of the values measured in the arcjet testing.

Table 1 RCC sample cases

Case designation	Case description	Computational methods used
1904	RCC testing	DSMC
1151	Hypervelocity impact testing	eDSMC, NS
2033	RCC testing	DSMC, NS

Table 2 Arcjet species and mole fractions

RCC case	1904 [a]	1151 [b]	2033 [b]
Species		Mole fractions	
N_2	0.565	0.182	0.177
O_2	1.07×10^{-4}	3.355×10^{-6}	0.033
N	0.103	0.568	0.551
O	0.328	0.250	0.239
NO	3.84×10^{-3}	2.49×10^{-6}	2.426×10^{-6}
Temperature, K	4934	900	929
Pressure, Pa	4335	141.6	151.07

[a]Stagnation conditions taken from the NATA solution downstream of the arcjet shock.
[b]Freestream conditions taken from the NATA conditions upstream of the arcjet shock.

The typical magnitude of the wall regression rate, when compared with the crack dimensions (from 1 to 50 mm), suggests that the material response and the gas-dynamic flows may be loosely coupled, thereby simplifying the wall damage modeling. Because it takes the gas less than 10^{-3} s to travel through the channel, it is reasonable to assume that the flow through the crack channel reaches a steady state at each of the various time-dependent channel geometries. This conclusion is reached regardless of the flow rarefaction for the three different cases considered here. In addition, it will be seen that, beyond a certain time, the flowfield itself is less sensitive to changes in the wall geometry because the flow chokes at the channel exit.

This surface model, which will be implemented in the three gas-dynamic approaches to be used, is simple and does not model surface catalycity. The degree of surface catalycity primarily affects the heat flux to the surface, especially for nonequilibrium flows. Gas-surface models are known with varying degrees of certainty, but for the RCC TPS material model there has been a large study of potential SiO_2-based reactions [14]. The level of agreement, however, obtained with the arcjet testing demonstrates that, for sufficiently damaged materials in an atomic oxygen environment (as would occur during reentry), the atomic oxygen interaction with carbon is the dominant mechanism.

B. Flowfield Modeling

The outcome of the gas-surface collisions given by Eq. (1) is modeled in each of the three computational methods employed in this work. The first two flowfield methods are kinetic methods known as DSMC and its collision-limiter version known as eDSMC. The DSMC method pioneered by Bird [13] is used for modeling rarefied flows in which computational fluid dynamics (CFD) approaches, based on the Eulerian and Navier–Stokes equations, do not hold due to the nonequilibrium nature of rarefied gases. The DSMC method is a statistical approach used to solve the Boltzmann equation, which describes the discrete nature of rarefied gases. Most DSMC algorithms require time and space discretization. The steps in such a discretization must be on the order of the time necessary for a molecule to collide and the mean free path of the molecules to ensure that the predicted flow parameters correspond to a solution of the Boltzmann equation. The values of the mean free path depend on the flow pattern; therefore, it is a good practice to choose the collisional cell size locally.

The second flowfield approach that we use in this work is an extension of the DSMC method for primarily inviscid, high-pressure flows, referred to as eDSMC. The approach is straightforward, involves considerably less computational cost than a DSMC calculation, and may be used to extend the DSMC method to regimes where kinetic effects are important. We denote the proposed equilibrium DSMC method as eDSMC, emphasizing that local equilibrium is the only assumption in the scheme. The eDSMC method is applied to high-pressure flows by using larger cells and time steps compared with what would be appropriate for the baseline DSMC method [6].

In the DSMC and eDSMC numerical calculations, the gas-wall reaction is implemented as follows. For each O-wall collision process, the reaction probability is compared with a random number. If the random number is less than the reaction probability, a CO molecule is released into the flow from the wall with full thermal accommodation boundary conditions. At the same time, the O atom that collided with the wall is removed from the computational domain. If the random number is greater than the reaction probability, the O-wall collision process does not result in a chemical reaction and the reflected O atom velocity and energy is calculated as it would be for other nonreactive species wall collisions. The effect of the nonreactive gas-surface collision is for the gas species to exchange momentum and energy with the wall. For true gas-surface collisions, a diffuse wall model with full accommodation is realistic, wherein the reflected molecular velocity is independent of the initial velocity and assumed to satisfy the equilibrium Maxwellian distribution.

The DSMC-based SMILE [15] code is used in this work to simulate microflows through the crack channel. The majorant frequency scheme and the variable hard sphere model (VHS) are employed for modeling molecular collisions. The Borgnakke–Larsen model is used to model energy exchange between the translational and internal models. The eDSMC code is based on a modification of the SMILE software as described in [6].

Finally, for the second and third RCC cases considered in this work, the pressure is sufficiently high such that an NS/CFD approach is applicable. For this reason, the General Aerodynamic Simulation Program (GASP) commercial CFD software is used to model the laminar NS solutions. The numerical solution of the Navier–Stokes equations for viscous flow is obtained by use of finite volume discretization of the computational domain. A no-slip boundary condition was used. In addition, a gas-wall boundary condition has been added to implement Eq. (1) for grid points adjacent to the wall.

III. Channel-Crack Configurations

The 1904 arcjet flow test with an initial rectangular crack channel in a carbon wall was modeled as a 2- and 3-D problem, as shown in Fig. 2. The cylindrical specimen sample has a diameter of 72 mm

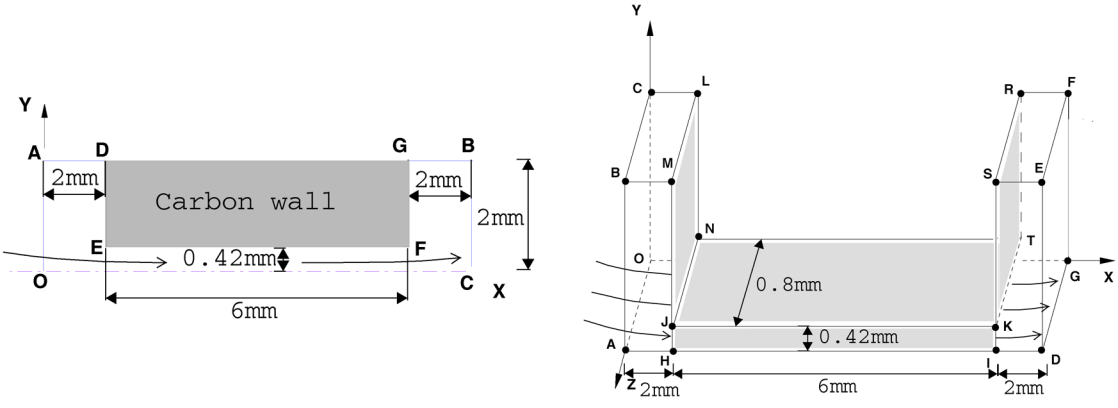

Fig. 2 Schematics of carbon channel configuration and boundary conditions for the two- and three-dimensional 1904 geometries.

facing the oncoming arcjet flow, with a thickness of 6 mm along the flow, streamwise X direction. Before arcjet exposure, the machined crack is a uniform rectangular channel of 0.84×36 mm in the YZ plane that is cut through the wall along the X direction. The carbon wall is supported by an insulated holder and connected to a thermal bath on the back surface by several bolts, with a constant back wall surface temperature of around 800 K. The center and corner portions of the channel flow were modeled separately as follows.

The flow at the crack center was modeled as a two-dimensional flow by neglecting the flow gradient in the Z direction. The computational domain OABC is shown in Fig. 2, in which DE and GF represent the front and back surfaces of the carbon wall, respectively, and EF represents the channel wall. Full thermal accommodation diffuse boundary conditions are used on the channel walls. To reduce computational cost, only half of the crack channel is simulated by using a specular boundary condition at the OCFG and ADGO planes. For collisions with a specular wall, the molecular velocity component normal to the surface is reversed, whereas the other two components parallel to the surface remain unchanged after reflection. Results for this flow configuration will be discussed in Sec. IV.A.1.

To further examine the surface regression rate around the corner of the channel, a 3-D DSMC calculation of the flow into and through the channel was modeled; the results will be discussed in Sec. IV.A.2. For this case, the impact of the side wall on the third direction, Z, was included. The geometry for the 3-D DSMC simulation and the computational domain of $10.0 \times 2.0 \times 0.8$ mm in the X, Y, and Z directions, respectively, are shown in Fig. 2. The front carbon wall facing the oncoming flow is simulated with a full thermal accommodation wall, MJNL at $X = 2.0$ mm, as is the back wall, SKTR at $X = 8.0$ mm. The gas at the stagnation conditions enters the computational domain through the inlet surface, OABC at $X = 0.0$ mm; flows through the channel defined by the walls HIJK and JNTK from $X = 2.0$ to 8.0 mm; and leaves the computational domain through the exit surface, DEFG at $X = 10.0$ mm. The top channel wall, JKTN at $Y = 0.42$ mm, and the side wall, HJKI at $Z = 0.8$ mm, are set with diffuse boundary conditions. To reduce computational cost, only half of the flow is simulated in the Y direction, the height of channel. In the Z direction along the channel width, we simulate a region with a distance of less than 0.8 mm to the side wall, JHIK. Thus, the symmetric surface, OADG at $Y=$ 0.0 mm, and the other surfaces (except the walls, inlet, and outlet boundaries) are set with specular boundary conditions. The streamwise flow velocity profiles obtained from the solution were shown in an earlier work [4] to have a parabolic shape, typical for Poiseuille flow, with a velocity slip observed at the wall increasing as the flow developed through the channel.

The layout of the 1151 case's computational domain, including the channel region, is presented in Fig. 3. The hypervelocity impact-damaged specimen is the assumed initial configuration in our calculations. Before testing in the arcjet, it has a diameter and depth of 6.5024 mm (0.26 in.) and 6.0 mm (0.23 in.), as may be seen on the left side of Fig. 1. The channel and external flow problems were coupled through the use of a computational domain designed to accommodate the bow and oblique shock wave structures as well as the interior of the channel and a portion of the flow inside the specimen. The eDSMC domain (shown by the outer rectangular box) is embedded in the nonequilibrium arc-tunnel analysis (NATA) computer code freestream conditions representative of the upstream arcjet shock conditions (see Table 2). The shaded area represents the sample holder with the circular hole shape (at the initial time) oriented normal to the incoming shock heated flow. The Mach number contours show the presence of the eDSMC simulated normal shock. Inside the circular RCC sample channel, the wall change is modeled by assuming a chemically active wall that reacts with atomic oxygen. A region downstream of the sample circular channel is also simulated.

Finally, Fig. 4a provides a schematic of the three-dimensional 2033 wedge case geometry. The rectangular crack has dimensions of 0.990×38.1 mm (0.0387×1.5 in.) with a depth of 6 mm. As in the 1151 case, the multiscale external–internal flow of case 2033 was

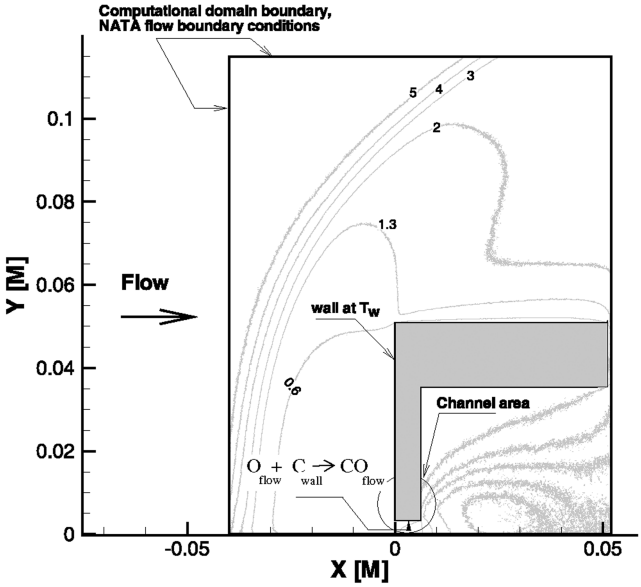

Fig. 3 Topology and boundary conditions of the 1151 computational domain. The contour levels indicate the flow Mach number. The wall at a temperature of T_w is diffuse with complete momentum and energy accommodation at the wall assumed.

solved using a computational domain constructed from several zones with different mesh structures. In this manner, we were able to accommodate the different flow phenomena, including the shock wave structure in front of the modeled portion of the space shuttle leading edge as well as the boundary layer inside the microchannel crack. The computational domain consisted of a larger outer subdomain, a tiny well-meshed microchannel, and a downstream subdomain at the exit of the specimen. Figure 4b shows an enlarged picture of the channel-area portion of the computational domain. To reduce computational effort, half of the three-dimensional flow in the channel was modeled making use of a symmetry plane.

IV. Results and Discussion

A. 1904 Results

The arcjet flow conditions and five chemical constituent mole fractions were taken from the NATA predictions of the arcjet postshock conditions and are given in Table 2. The arcjet expands in a vacuum environment, forms a normal shock in front of the cylinder body front surface, then penetrates through the crack channel. The NATA postshock conditions are assumed at the DSMC AO computational boundary 2 mm upstream of the channel inlet (see Fig. 2). The arcjet gases also flow around the carbon wall and form a gas environment surrounding the wall back surface. The NS solver GASP [16] was used to predict a crack exit pressure, Mach number, and temperature of 40 Pa, 1.5, and 800 K, respectively, for the DSMC calculation exit conditions [17].

The mean free path of the gas molecules at the channel inlet is about 0.02 mm. Taking the channel dimension in the Y direction as the characteristic length, the Knudsen number distribution along the channel center line varies from 0.024 at the flow entrance to about 0.5 at the exit (see Fig. 6 of [4]). To minimize computational cost, the flow through the crack can be reduced to a 2-D problem in the center region cross section of the channel because the dimension of the crack cross section normal to the Z direction is more than 40 times greater than the value in the Y direction. To examine the flow and surface regression near the channel corner, however, a 3-D DSMC simulation will be performed.

1. Two-Dimensional Flow at the Crack Center

The 2-D DSMC simulations are summarized as follows. An orthogonal mesh with square cells was used in the simulation with 80 and 400 cells in the Y and X directions, respectively.

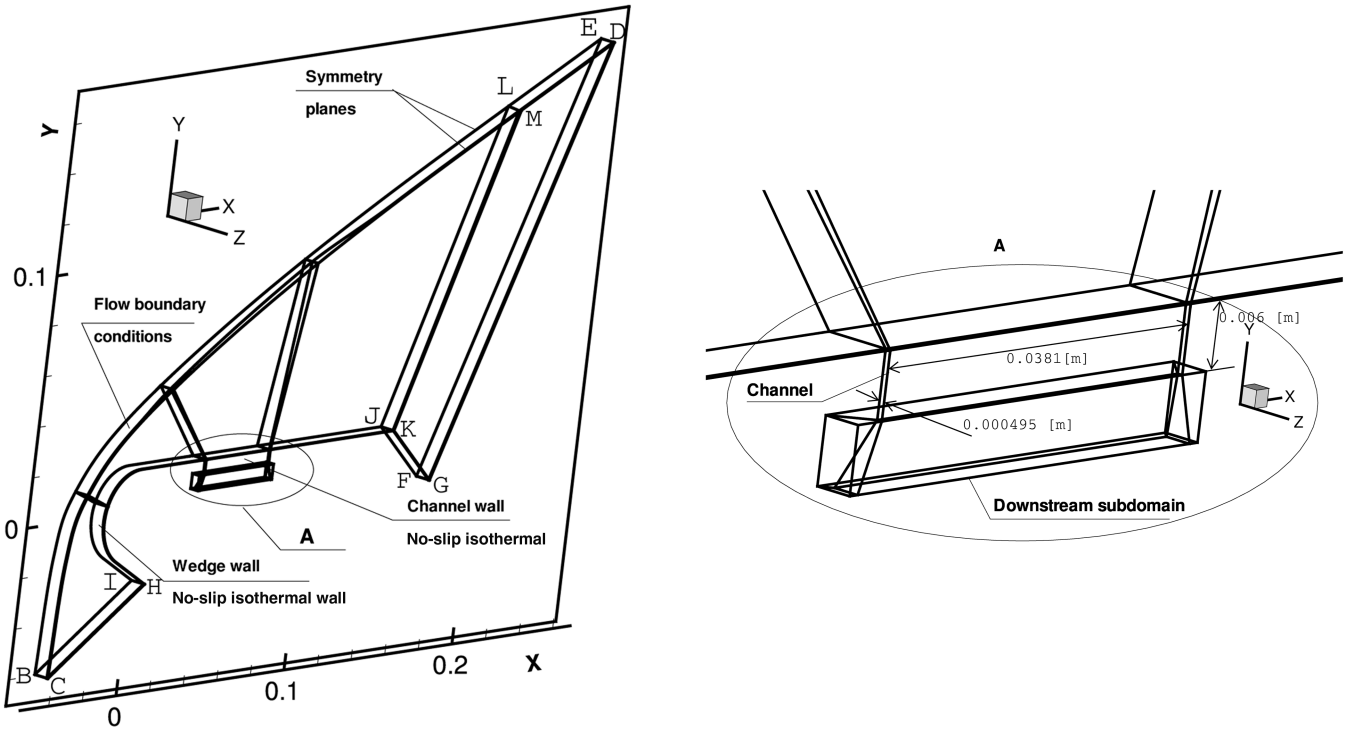

Fig. 4 Topology and boundary conditions of the 2033 computational domain.

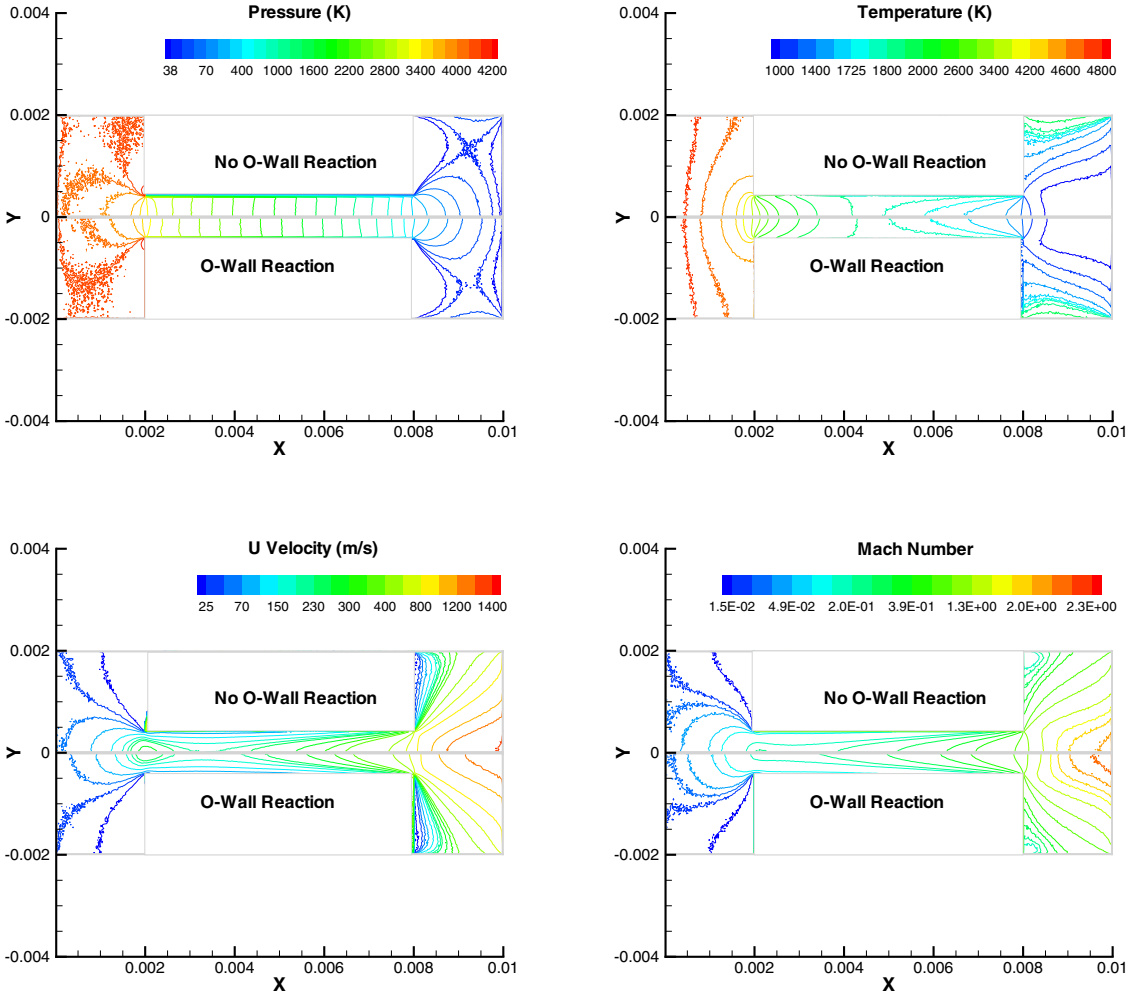

Fig. 5 Comparison of distributions along the initial rectangular channel for the simulations with and without reactions between O species and the wall: a) pressure, b) temperature, c) streamwise velocity, and b) Mach number.

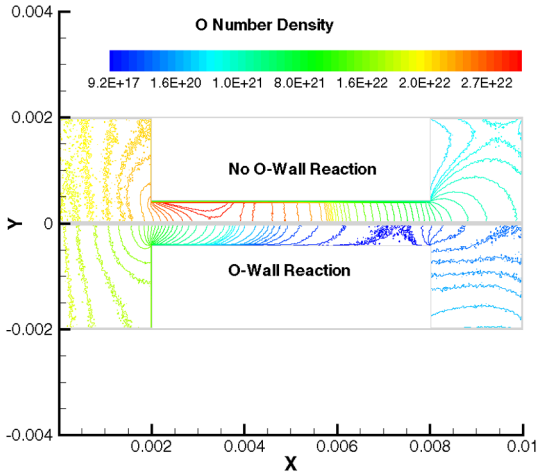

Fig. 6 Comparison of O number density along the initial rectangular channel for the simulations with and without reactions between O species and wall.

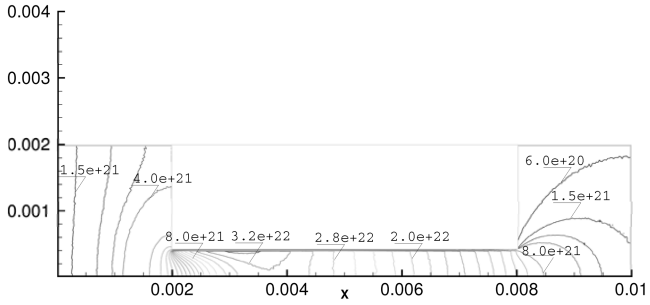

Fig. 7 CO number density along the initial rectangular channel for the simulation with O-wall reactions.

Using an adaptive grid technique, each cell can be divided up to 10 times according to the flow gradients obtained during the simulation. The number of cells was found to increase from 32,000 to 135,000 after the flow reached the steady state. A time step of 1.2×10^{-7} s was used in the simulation, and the number of real molecules represented by a simulated particle, F_{num}, was chosen as 4.0×10^{11} in the simulations. The flow was assumed to have reached the steady state after the 1500 time steps. About 1,000,000 simulated molecules were used to represent the gas at steady state. The DSMC simulation results are sampled from the 1500th step until the 16,000th time step, and a typical calculation took about 32 h on 18 parallel Advanced Micro Devices, Inc., 1526 MHz Athlon processors.

Figure 5 compares the flow macroscopic contours of pressure, temperature, streamwise (x-component) velocity, and Mach number for the simulations with and without the gas-surface chemical reaction according to Eq. (1). For the simulation without the gas-surface reaction, the O particles are reflected back into the flow after collisions with the channel wall EF. In contrast, for the simulations with the gas-surface reaction, 90% of the O atoms combine with wall carbon atoms after they collide with the channel wall, and the newly generated CO molecules are released into the flowfield. The change in the chemical constituents in the channel flow between the simulations with and without the gas-surface reaction is noticeable in the pressure and streamwise velocity. The presence of the CO molecules, heavier than O atoms, increases the pressure and decreases the streamwise velocity for the simulations that incorporate the gas-surface reaction. Note that the difference in the flowfield temperature between the simulation that included the wall reaction and the one that did not is not significant due to the same full thermal accommodation boundary condition. Figure 6 compares the contours of O number density between the simulations with and without gas-surface reactions and shows that, for the probability of 0.9 assumed here, O particles are largely consumed in the simulation that models the gas-surface reaction. The number density contours of carbon monoxide, generated by the gas-surface reaction, are shown in Fig. 7. Although the CO molecules can only be generated in the channel, they are also observed upstream of the channel inlet due to the subsonic nature of the flow. The regression rate of the carbon wall due to the O-wall reaction for the rectangular channel is shown in Fig. 8a. The three profiles correspond to simulations performed for three different arcjet exposure times. It can be seen that the regression rate decreases exponentially along the flow direction to almost zero at the wall located 3 mm beyond the entrance because most of the O atoms have been consumed in the first half of the channel. Assuming that the local carbon wall regression rate is constant for a period of time, a new channel shape may be obtained (Fig. 8b) and new DSMC flowfield calculations are performed for the expanding channel. The new flowfield generates a new channel wall regression rate profile and is shown at a subsequent wall regression time of 10 s (the 10 s curve in Fig. 8a). Then the entire process is repeated to obtain the curve labeled 50 s. Note that better numerical accuracy could be obtained by iterating more frequently or at decreased physical time intervals. In any case, the flow is assumed to reach the steady state for each channel geometry because it takes less than 10^{-3} s for the flow gas to travel through the entire channel. During such a short period of time, the change in the wall regression rate can be neglected.

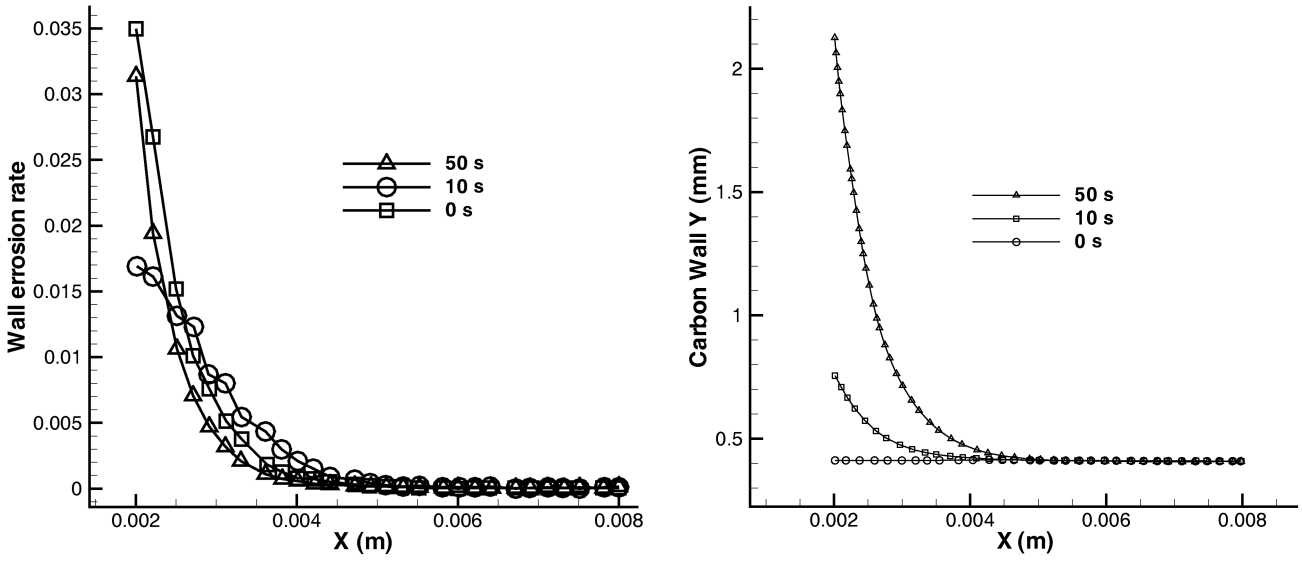

Fig. 8 Distance through the channel at various times due to O-wall reactions: a) carbon wall consumption rate, and b) channel shape.

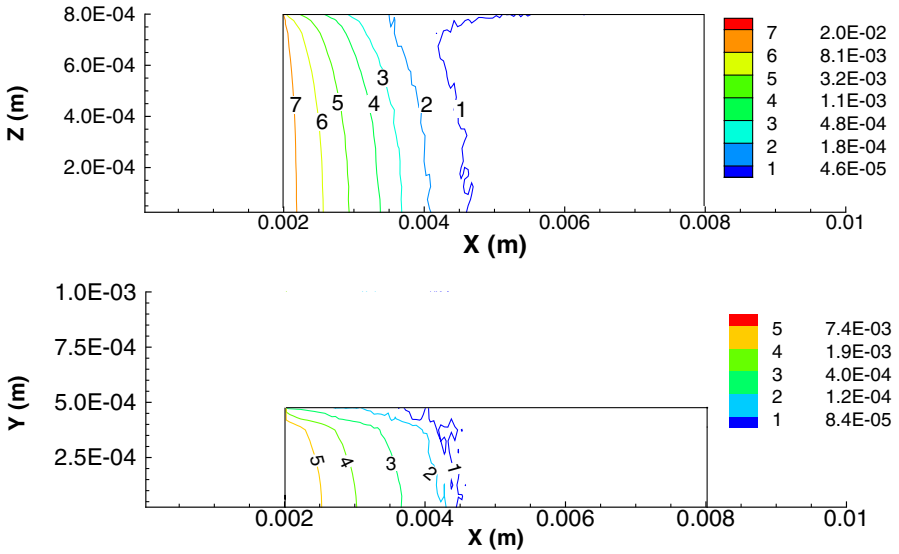

Fig. 9 The regression rates (in millimeters per second) from the 3-D simulation: a) wall JKTN, and b) side wall JKIH.

A comparison of the flow pressure, temperature, streamwise velocity, and Mach number along the channel centerline at 0, 10, and 50 s shows that, although the channel entrance dimension may increase fivefold during the 50 s, the flowfield profiles do not significantly change during this time because the flow always accelerates to the sonic speed at the channel exit. This lack of change in the flowfield parameters is consistent with the lack of variation of the regression rate profile through the channel (Fig. 8a). From these results, we may conclude that the entrance of the channel approximately expands at a constant rate because the mass flow rate of the atomic oxygen remains relatively constant due to the choking of the flow at the channel exit [17].

2. Three-Dimensional Flow at the Crack Corner

The regression rates (in millimeters per second) of the wall JKTN and the side wall JKIH from the 3-D simulation are shown in Figs. 9a and 9b, respectively. It can be seen that, along the flow direction, the regression rate decreases exponentially on both walls due to the consumption of O species, and there is almost no wall consumption beyond 0.005 m. At the entrance, the corner top wall, JKTN, has a regression rate of about 0.02 mm/s, which is on the same order of the regression rate at the channel center obtained from the 2-D calculations. The side wall JKIH has a rate about 3 times less than the value on the JKTN wall. The similarity of the rates at the crack-channel center and the corner suggests that the flow expands evenly in all directions, producing the change from the rectangular to the circular shape seen in the arcjet after 900 s of testing [5].

B. Results of the 1151 Case

The eDSMC axisymmetric calculations were performed with a nonuniform orthogonal computational mesh for the computational domain shown in Fig. 3. The initial mesh of background cells consisted of 150 × 100 cells with subdivisions of up to 15 subcells in each direction allowed. The subdivisions are a form of adaptive gridding and occur in areas with high flow density gradients. These areas included the channel because it is located in the stagnation region of the flow. The final steady-state mesh consisted of approximately 512,000 cells and 8,113,000 computational particles.

1. Comparison of Initial Configuration for eDSMC Flow Solutions with and Without Gas-Surface Chemistry

To understand the influence of the gas-channel wall reaction on the local flow conditions, we performed calculations for the initial configuration of the channel with and without wall chemistry. In both cases, the flow-wall nonreactive boundary conditions are diffuse with total energy and momentum accommodation. Similar to the 1904 case, the flow is Poiseuille in nature, except that the smaller channel aspect ratio creates a flow that is not fully developed. Unlike the 1904 case, which is a higher Knudsen number flow, the larger 1151 channel flow is a higher-pressure channel flow. Its correspondingly thinner boundary layer has the affect of permitting more atomic oxygen penetration to the wall as a function of distance along the channel centerline. Figures 10–14 present a comparison of total flow mass density, pressure, temperature, and streamwise velocity, respectively, along the channel wall for the eDSMC cases with and without the reacting wall. As can be seen in the figures, the temperature and pressure profiles remain the same in both of the cases whereas the density and velocity profiles are somewhat different. The heavier CO molecules can penetrate the flow upstream (through the subsonic boundary layer), increasing the flow density in front of the specimen. The velocity boundary layer in the case of the chemically active wall is thicker again due to the presence of the heavier CO molecules that tend to remain in the channel longer than the other, lighter species. Figure 14 presents the difference in the atomic oxygen mass fraction distributions for cases with and without the reacting wall. A larger concentration of atomic oxygen at the channel wall in the channel is evident for the case of the nonreacting wall.

2. Loosely Coupled Gas and Channel Shape eDSMC Flow Calculation Results

A series of eDSMC calculations were undertaken to predict the hole growth process observed in the hypervelocity impact experiments [5] that lasted 450 s. Starting with the initial geometric

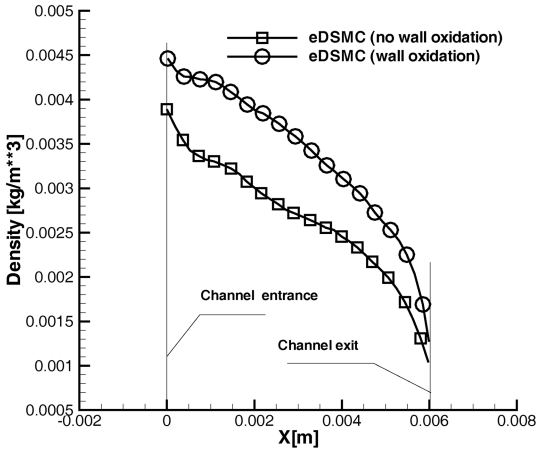

Fig. 10 Comparison of eDSMC mass density profiles along the channel wall for gas-wall oxidation reactions vs no gas-wall reactions (dimensions are in meters).

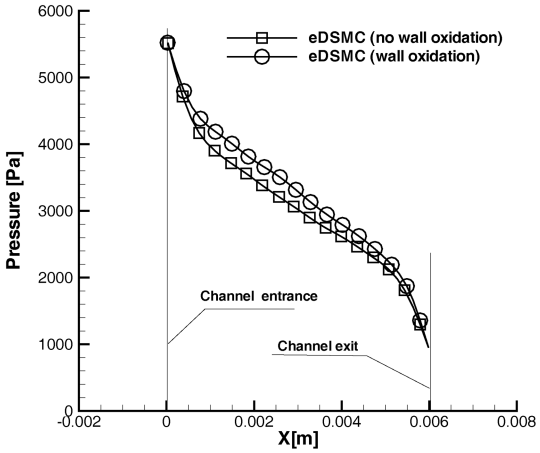

Fig. 11 Comparison of eDSMC pressure profiles along the channel wall for gas-wall oxidation reactions vs no gas-wall reactions (dimensions are in meters).

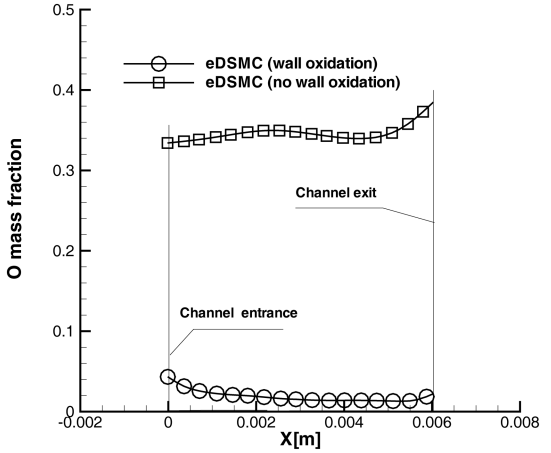

Fig. 14 Comparison of eDSMC atomic oxygen mass fraction profiles along the channel wall for gas-wall oxidation reactions vs no gas-wall reactions (dimensions are in meters).

configuration of the channel (a tube), we calculate the wall oxidation rate along the channel and use this rate to increase the channel hole diameter. Because the oxidation rate is nonuniform along the channel, the geometric profile of the channel changes as the wall material is consumed. The time between two sequential eDSMC simulations corresponded to 50 s and, during that time, we assumed that the rate of carbon loss was constant. To better resolve the wall profile change in between successive eDSMC simulations, the following procedure was adopted. The local wall recession rate was computed and fixed for each of the surface mesh vertices. The wall profile change was computed incrementally according to the local recession rate with a time step of 5 s. After each 5 s increment, the

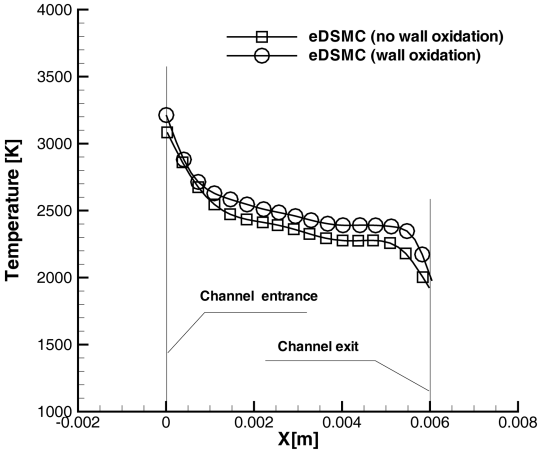

Fig. 12 Comparison of eDSMC temperature profiles along the channel wall for gas-wall oxidation reactions vs no gas-wall reactions (dimensions are in meters).

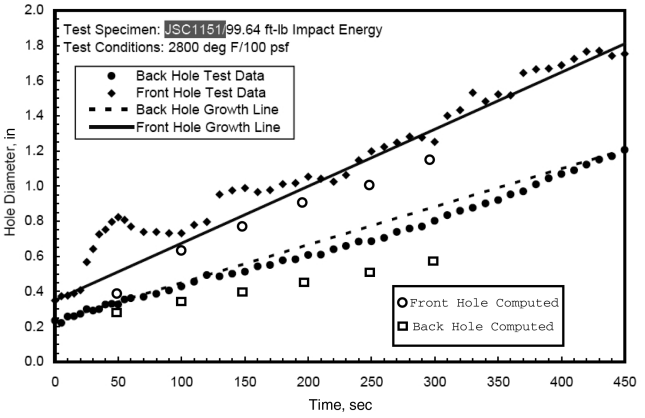

Fig. 15 Comparison of measured and computed hole growth diameter for 1151 hypervelocity impact arcjet damage testing. Simulated hole diameters are indicated as open symbols.

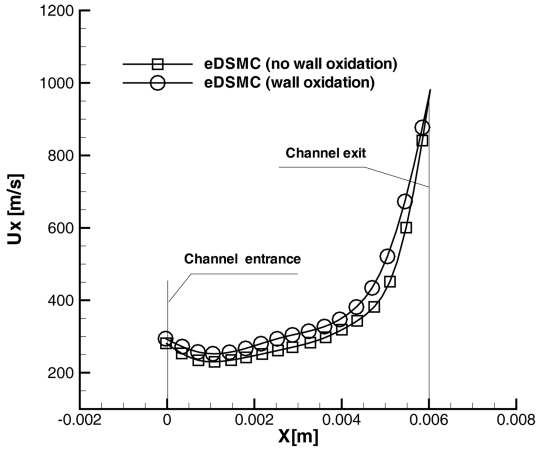

Fig. 13 Comparison of eDSMC *X*-velocity profiles along the channel wall for gas-wall oxidation reactions vs no gas-wall reactions (dimensions are in meters).

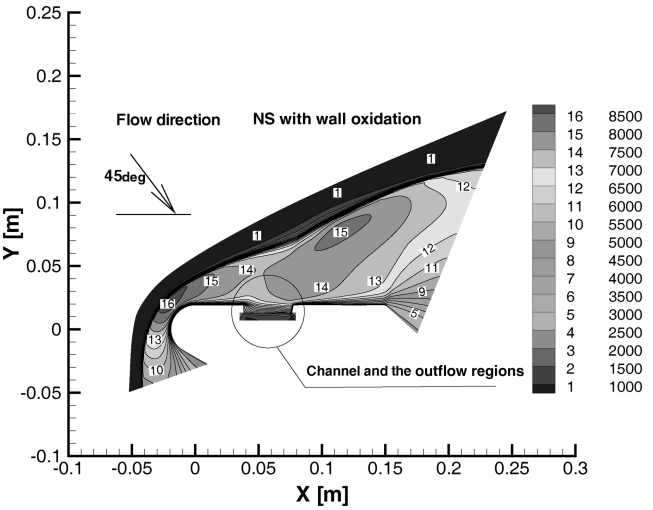

Fig. 16 Temperature distributions for the external wedge flow with and without wall oxidation in the channel. The internal flow corresponds to 20 s of wall oxidation inside the channel.

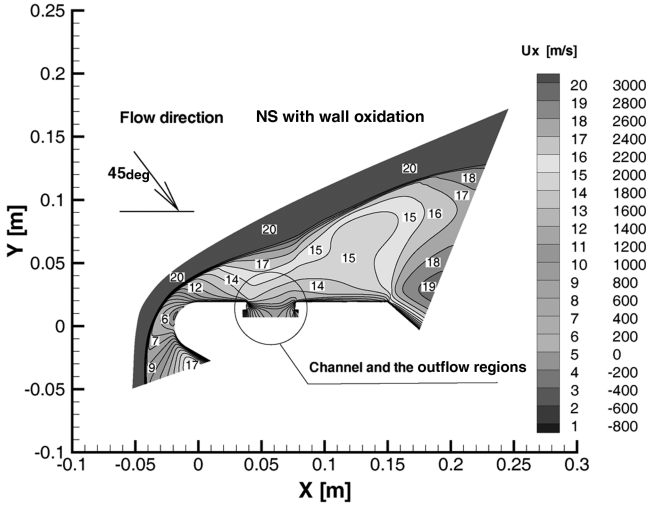

Fig. 17 ***X*-velocity distributions for the external wedge flow with and without wall oxidation in the channel. The internal flow corresponds to 20 s of wall oxidation inside the channel.**

surface normal direction was recomputed and used for the next calculation of the local wall surface normal direction. This procedure allowed for a more accurate determination of the wall *shape change* than if the surface normals were computed only once at the beginning of each 50 s time interval between eDSMC calculations. The eDSMC calculations were repeated six times to simulate the experimental arcjet exposure for 300 s.

The result of these loosely coupled calculations is the prediction of hole diameter along the channel centerline. We compare the computational results for the channel inlet and outlet hole diameters as a function of time with the experimental results in Fig. 15. The open symbols are the eDSMC-predicted hole diameters at the windward (or hole forward surface) and the leeward (or hole back surface), respectively. The modeling predicts smaller hole diameters, particularly at the channel exit, than the experiment. However, the predicted trend is seen to be very close to the experiment. One reason for the remaining discrepancy is experimental error in determining the hole diameters due to difficulty in reading the imagery taken during the test (note that at the initial time the front and rear hole diameters should be identical). Another reason is that the geometry modeled is representative of the test, but idealized. Close examination of the images of the sample presented in the second and third rows of Fig. 1 before arcjet testing shows that there is imperfect removal of the silicon carbide/carbon layer by the hypervelocity impact (see the speckled region around the hole). Therefore, there is probably more atomic oxygen penetration than we have accounted for. Finally, the use of Navier–Stokes with slip correction may provide a more accurate boundary-layer solution than eDSMC; however, comparisons of the wall oxidation rate for the initial geometry obtained with eDSMC and NS solutions were found to be similar [4].

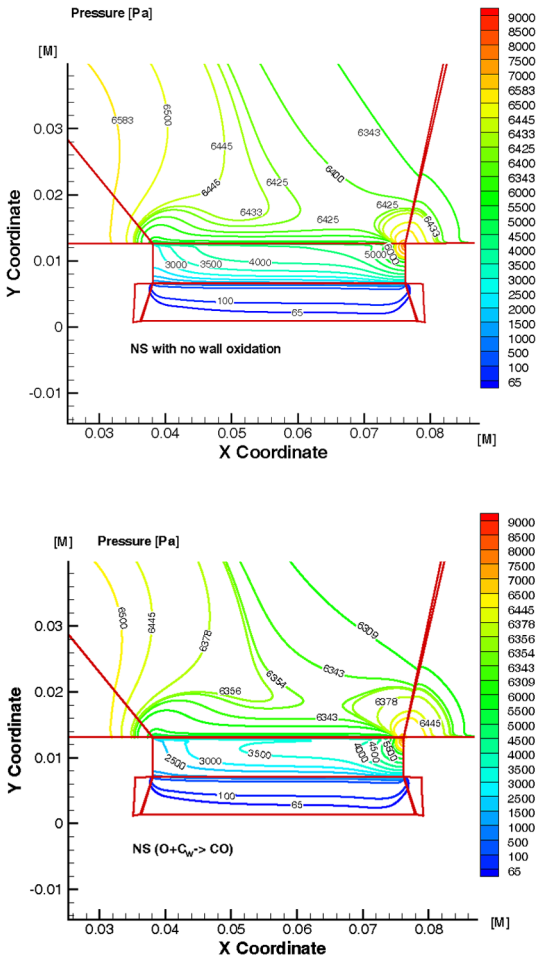

Fig. 18 Comparison of pressure distributions for the wedge channel flow with and without wall oxidation in the channel, $Z = 0$.

C. Results of the 2033 Case

In this subsection, we discuss the NS calculations that were performed to analyze the flow physics and mechanisms for material

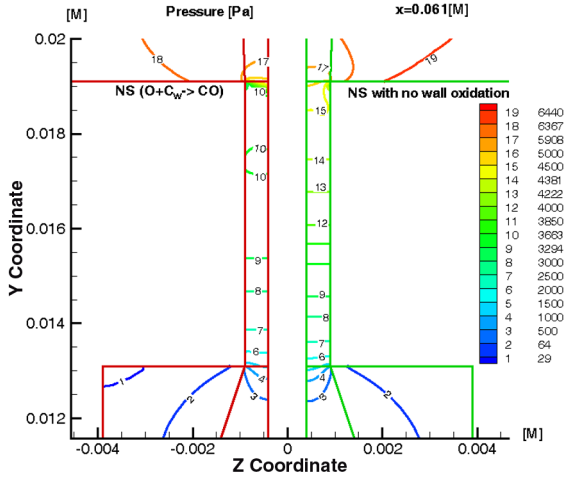

Fig. 19 Comparison of pressure distributions for the wedge channel flow with and without wall oxidation in the channel, *ZY*-plane view, $X = 0$.

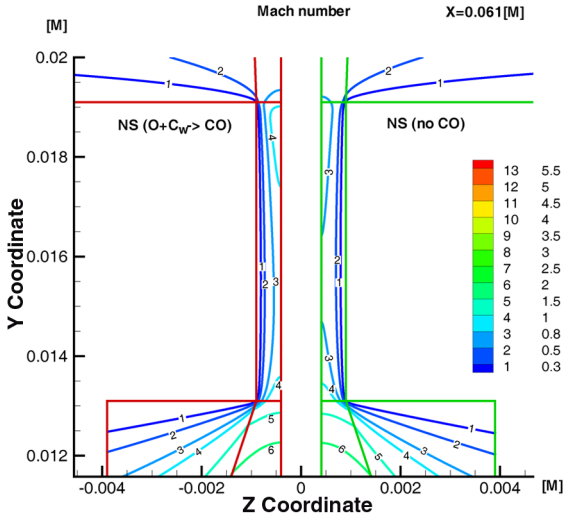

Fig. 20 Comparison of Mach numbers for the wedge channel flow with and without wall oxidation in the channel, *ZY*-plane view, $X = 0$.

regression for the 2033 arcjet wedge test. The NS calculations were performed based on the computational domain presented in Fig. 4a. A three-dimensional block structured multizone mesh was created using the GASP software, and the entire computational domain consisted of 3,966,256 mesh points. A typical zone is marked on Fig. 4a as ED–LM–JK–FG. The freestream uniform boundary conditions obtained from the NATA solution (see Table 2) were applied along the curved inlet surface BC–ED. The computational domain accommodates bow and oblique shock waves in front of the specimen. The inlet surface is aligned with the shock wave structure to reduce the size of the computational domain. First-order extrapolation boundary conditions were applied at the surfaces BC–HI, JK–FG, and FG–DE, whereas the no-slip temperature conditions were applied along the surface JK–HI, except for the entrance of the channel where point-to-point correspondence was maintained with the computational zone adjacent to the interior of the channel.

Simulations were performed with and without wall oxidation chemistry, a two-dimensional approximation to the true three-dimensional geometry, and loosely coupled with the wall shape change. The analysis of the dimensionality of the problem allowed us to simplify the full three dimensionality, as was necessary to evaluate the material shape change. Finally, the change in the shape of the sample as well as the oxidation rate is compared with the arcjet result.

Figures 16 and 17 show the predicted temperature and x-velocity contour fields with wall chemistry for the flow external to the channel. Similar calculations performed without wall chemistry showed that the contour fields of the external flow were the same and were unaffected by the channel wall-gas chemistry, as might be expected. The shock wave structure, including the bow shock in front of the channel as well as the oblique shock along the specimen wall may be observed in the contour plots shown in the figures. Figure 16 shows a significant increase in the temperature after the shock (from 900 to approximately 8000 K), corresponding to the decrease of velocity from about 4000 m/s to stagnation, seen in Fig. 17. The temperature decrease close to the specimen wall is due to the velocity and temperature no-slip conditions for a specimen wall set to the experimental value of approximately 1800 K.

1. *Effect of Wall Chemistry Inside the Channel*

The effect of chemistry on the flow in the vicinity of and inside the channel is considered here. Except for the conditions at the channel walls, all the other boundary conditions, including flow conditions, are the same. With respect to the macroparameters inside the channel,

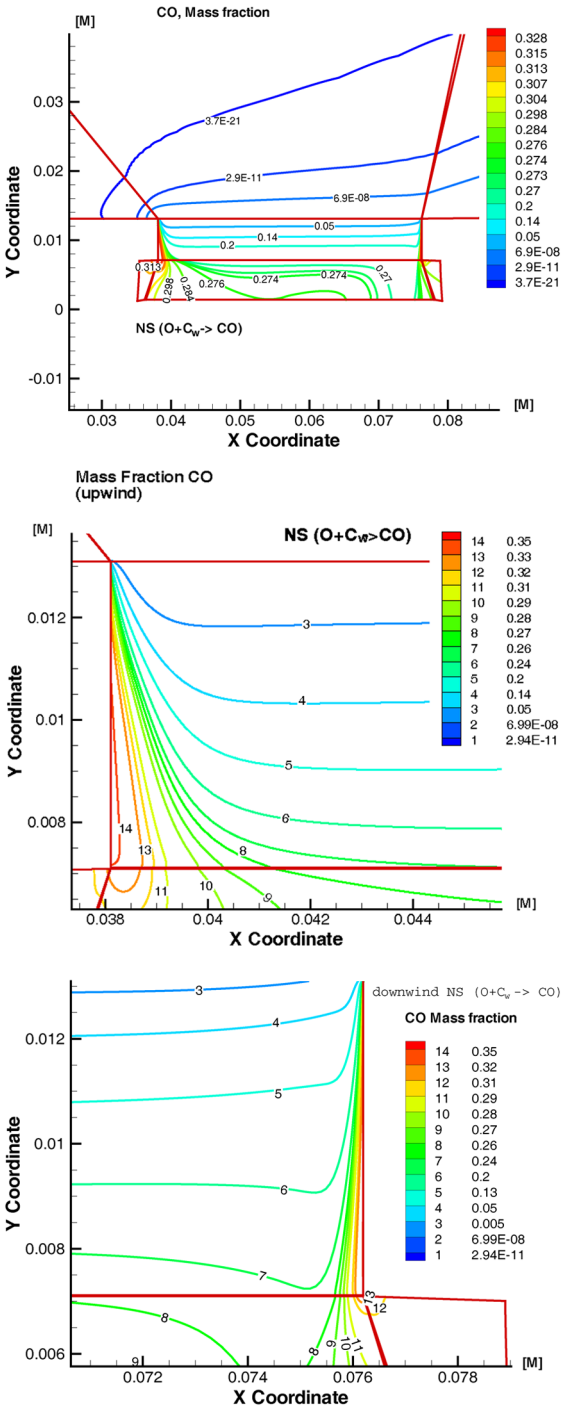

Fig. 21 CO mass fraction distributions for the wedge channel flow in the channel, $Z = 0$: a) entire channel flow, b) enlargement of upwind channel region, and c) enlargement of downwind channel region.

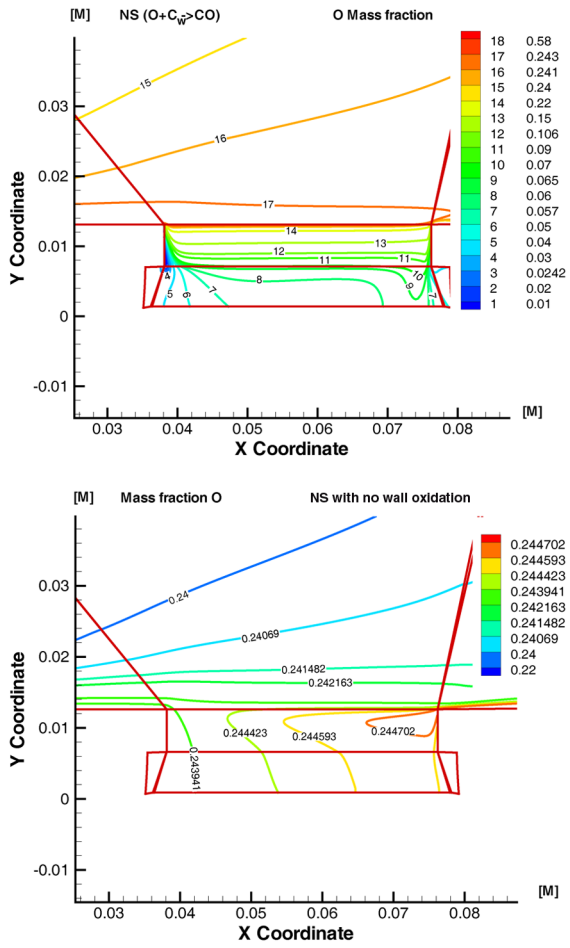

Fig. 22 Comparison of atomic oxygen mass fraction distributions for the wedge channel flow with and without wall oxidation in the channel, $Z = 0$.

the pressure distribution shows the largest difference in spatial variation for cases with and without wall oxidation. Mach number, for example, was found to be relatively insensitive to the use of the wall oxidation model. Figure 18 shows a comparison of the pressure contours with and without wall oxidation in the channel. The presence of wall chemical reactions causes about a 10% difference in the pressure contour values inside the channel with the highest pressure change observed at the upstream corner of the flow (see location $X = 0.075$, $Y = 0.012$). The influence of the wall oxidation model can be seen more dramatically in a ZY plane of the channel flow, as shown in Fig. 19. It can be observed in the right portion of the figure that, for the wall oxidation case, the pressure gradients are higher at the entrance of the channel, and the pressure value is generally lower in the channel solution with the reactions at the wall. However, for both cases, the pressure values become equal at the exit of the channel as the Mach number approaches unity (see Fig. 20) and the flow chokes.

The effect of CO production due to the carbon wall oxidation process affects the flow gas dynamics. Figure 21 shows the CO mass fraction distributions in the XY cross section of the wedge channel flow in the channel. Shown in Figs. 21a–21c are the CO distributions for the entire channel flow and an enlargement of the upwind and downwind channel flow regions, respectively. It can be observed that mass fraction of CO, which is the product of the wall oxidation process, is larger at the upwind wall of the channel. Examination of a YZ cross section (not shown) demonstrates that the CO molecules create a thick boundary layer along the channel side walls. The enlargements of the XY cross-sectional views show that there is a larger concentration of CO at the upwind channel wall because it is less exposed to the oncoming oxygen from the flow over the wedge specimen. This result can be understood in that the CO molecules have a larger residence time in the vicinity of the upwind channel wall, again, because they are in the lee of the incoming flow into the channel. The difference in the spatial distribution of the atomic oxygen mass fraction for channel flow solutions with and without wall oxidation rate may be seen in Fig. 22. Figure 23 also shows an enlargement of the upwind and downwind wall regions for the channel flow with wall oxidation. It can be seen that the mass fraction of oxygen in the case with wall oxidation is lower at the upwind wall of the channel than at the downwind wall. This occurs because a larger portion of CO remains in the region at the upper wall and tends to force the other components (including atomic oxygen) out of that region. This effect can actually shield the upwind wall from the impacting oxygen, thus preventing the subsequent destruction of the wall.

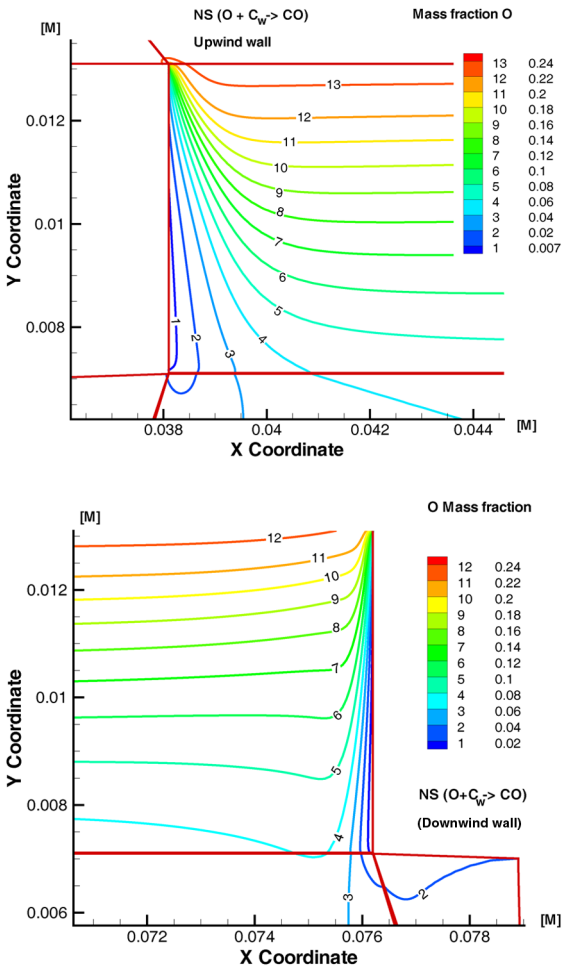

Fig. 23 O mass fraction distributions for the wedge channel flow, with wall oxidation, in the channel, $Z = 0$: a) enlargement of upwind channel region, and b) enlargement of downwind channel region.

2. *Flow Dimensionality*

The 2033 wedge flow is a truly three-dimensional flow, as discussed earlier. However, to understand the importance of modeling the three dimensionality, the flow through a two-dimensional geometry (ignoring the side walls) was also investigated. A wider channel in the 2-D case produces an additional shock wave that interacts with the oblique shock wave over the specimen. Mach number contours (see [4]) show that a shock wave is formed over the downwind wall of the channel. Unlike the 3-D case, the 2-D results show no difference in

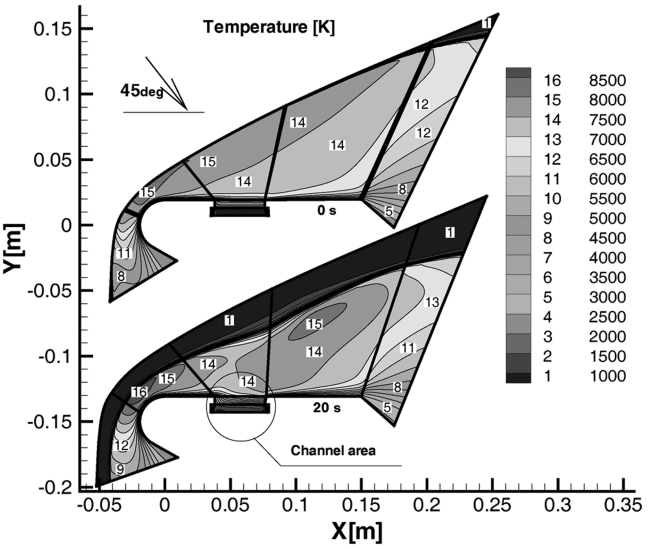

Fig. 24 Comparison of linearized 3-D temperature profiles at the initial and a later time for the external wedge flow.

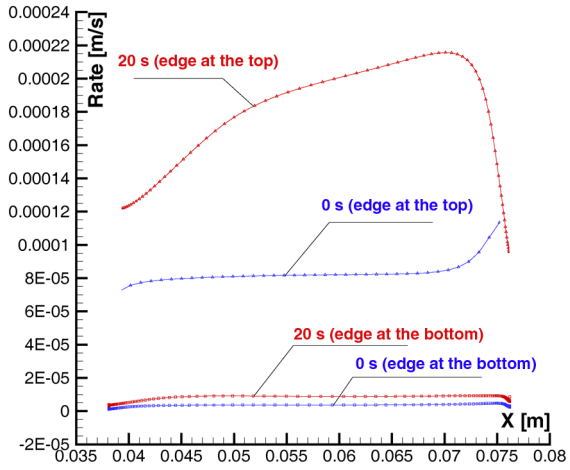

Fig. 25 Wall regression rate along the outer and inner edges of the channel, 20 s into the experiment.

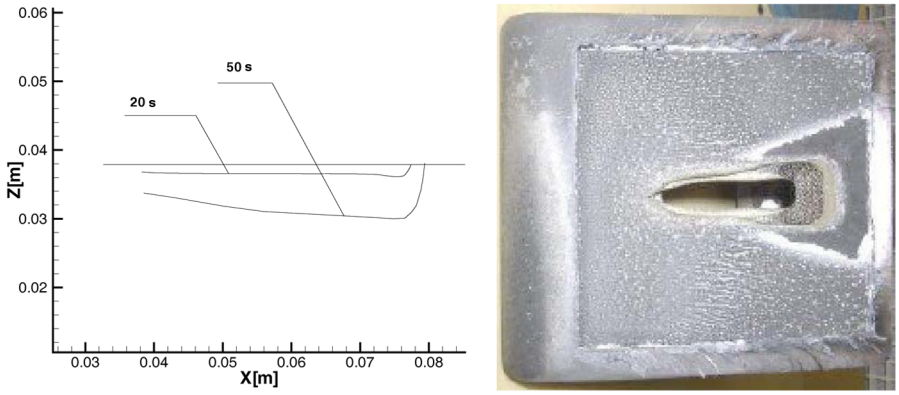

Fig. 26 Shown are the following: a) wall regression rate at different times, and b) arcjet damage sample (RHS) with a final posttest penetration of dimension 0.47 × 2.42 in.[2]

the CO mass fraction at the upwind and downwind walls of the channel. The 3-D simulation shows that the flow is influenced by the channel side walls, particularly the atomic oxygen mass fraction and the predicted wall regression rates. It was found, however, that the oxidation rate at the entrance of the channel predicted by the 2- and 3-D NS is actually close. Therefore, an approximate two-dimensional calculation would at least provide an estimate of the *worst case* destruction rate. The dimensionality analysis also suggests that, once the channel gets larger, the 3-D flow pattern resembles the 2-D solution, because the influence of the side walls becomes weaker. This, in turn, suggests that for the purposes of the loosely coupled flowfield-wall shape iterations a two-dimensional approximation to the geometry is reasonable.

3. *Flowfield and Channel Shape Iterations for Case 2033*

A series of iterations at 0, 20, and 50 s were performed with the approximate linearized three-dimensional geometry shown in Fig. 4b. Figure 24 shows a comparison of temperature contours at the initial and a later time for the external wedge flow. It may be seen in the figure that as the channel grows it begins to influence the outer flow pattern. A second shock wave starts forming as the channel size grows and, as mentioned earlier, the flow pattern comes closer to the 2-D solution. The oxidation rate along the side wall at the top and bottom of the channel at 0 and 20 s is presented in Fig. 25. As the channel grows larger, the oxidation rate increases due to the better ability of the flow to penetrate through the channel and the rate increases more at the inlet to the channel than at the exit.

Figure 26 shows a top view of the wall regression rate for the three iterations performed. The simulation results are presented in Fig. 26a, and the arcjet result is shown in Fig. 26b. The obtained channel shape is close to that experimentally observed. Table 3 presents the calculated mass flow rates as the channel grows. The increase of the oxidation rate for the outer edge approximately follows the increase of the mass flow through the channel. At the current rate, the final channel width would be approximately twice as large as that observed in the experiment. This overestimate of the experimentally observed oxidation rate is due to the adopted linearized approach to the geometry modeling (see Fig. 4b). The linearization of the geometry makes it easier for the flow to penetrate through the channel. However, the general shape change is amazingly consistent with the arcjet result, suggesting that the dominant flowfield and gas-wall interactions have been captured.

Table 3 Case 2033 wedge channel mass flow rates

	0 s	20 s
Area, m^2	1.88×10^{-5}	8.04×10^{-5}
Total mass flow, kg/s	4.77×10^{-5}	9.72×10^{-5}
Mass flow of O, kg/s	1.12×10^{-5}	2.33×10^{-5}

V. Conclusions

In this work, an approach was developed to model transitional through continuum flows through carbon-crack channels of RCC test sample geometries. The gas dynamics were modeled using different flowfield modeling techniques, including DSMC, a collision-limiter version known as eDSMC, and NS. The selection of the specific flowfield model was case dependent because the freestream Knudsen number widely varied among the three cases. For all three flowfield models, the same physical mechanism for the carbon wall consumption was employed. Atomic oxygen impacting a bare carbon wall is assumed to chemically react with the wall to produce CO gas that enters the flowfield. The probability of the reaction was the only parameter in the model, with a value of 0.9 used in all simulations. It was found that atomic O carbon surface consumption accounts for a large mass loss and produces a shape similar to the arcjet sample for all three cases.

For the 1904 arcjet case, it was found that the flow is transitional, chemical reactions in the gas phase flow through the channel are not important, and the velocity distributions follow the usual Poiseuille flow with slip observed in microchannel calculations. The results were also relatively insensitive to the reaction probability, and the wall regression rates calculated with the 2- and 3-D DSMC approaches were similar. The DSMC simulations predict carbon channel wall regression rates that are consistent with the arcjet experimental data.

For the second configuration considered, 1151, the carbon oxidation rate calculations show that the variation along the channel wall is different from the 1904 stagnation test. The freestream pressure for this case is higher, making a DSMC calculation unfeasible so that the eDSMC and NS approaches were considered. In contrast to 1904, the larger 1151 circular channel supplies more atomic oxygen for the gas-wall reaction to occur and the availability of atomic oxygen to drive the wall reaction is less important in terms of the oxidation rate further downstream. The eDSMC-calculated front hole growth through 300 s shows a good level of agreement with the general trend of the experimental data, given the experimental uncertainties in the data. The consideration of nonidealized geometry affects might improve the already good agreement between the modeling and experiment further.

For the arcjet wedge case (2033), the flow is entirely in the continuum regime and, to provide a full 3-D solution, an NS computational tool with wall oxidation is required. The effect of wall oxidation on the external and internal channel flow was examined as well as the dimensionality of the problem. Local gas flowfield results were found to affect the oxidation rate in a manner that cannot be predicted by previous mass loss correlations. For example, the longer residence time of the CO gas component at the upwind wall of the channel was found to create a shielding effect, which tends to reduce the upwind wall oxidation rate. The flow inside the channel was affected by the presence of the channel side walls, but if an estimate of the maximum destruction rate is desired, a 2-D consideration of the flow may be used. The study of the flow dimensionality suggested

that the complexity of the gas-dynamic-wall shape iterations could be simplified by linearizing the channel geometry. This approach gives larger oxidation rates than observed in the experiment because it is easier for flow to penetrate the channel. Improved geometry meshing techniques will be considered in the future to enable a full three-dimensional simulation.

Acknowledgments

E. V. Titov, J. Zhong, and D. A. Levin would like to acknowledge support from Boeing contract no. 6H08845. Special thanks are due to M. Ivanov of the Institute of Theoretical and Applied Mechanics, Russia, for the use of the original SMILE code. We would especially like to thank the AeroSoft Corporation, Blacksburg, Virginia, for their technical support and assistance in incorporating the gas-wall oxidation boundary condition. All of the authors would like to thank D. Curry and A. Rodriguez for their programmatic and technical support as well as their encouragement and interest in this project. Thanks are also due to Max Larin and Brian Anderson for their help in providing NATA predictions of the arcjet conditions as well as DPLR comparison flowfields.

References

[1] Curry, D. M., Pham, V. T., Norman, I., and Chao, D. C., "Oxidation of Hypervelocity Impacted Reinforced Carbon–Carbon," *Journal of Spacecraft and Rockets*, Vol. 37, No. 3, 2000, pp. 310–317. doi:10.2514/2.3580

[2] Williams, S., Curry, D., Chao, D., and Pham, V., "Ablation Analysis of Shuttle Orbiter Oxidation Protected Reinforced Carbon–Carbon," *Journal of Thermophysics and Heat Transfer*, Vol. 9, No. 3, July–Sept. 1995, pp. 478–485. doi:10.2514/3.690

[3] Tang, C., Saunders, D., Trumble, K., and Driver, D., "Rapid Aerothermal Simulations of Damage and Repair During a Space Shuttle Mission," AIAA Paper 2007-1783, April 2007.

[4] Titov, E., Zhong, J., Levin, D., and Picetti, D., "Simulation of Crack Growth Due to Carbon Oxidation in High-Temperature Gas Environments," AIAA Paper 2007-4469, June 2007.

[5] Curry, D. M., Pham, V. T., Norman, I., and Chao, D. C., "Oxidation of Reinforced Carbon–Carbon Subjected to Hypervelocity Impact," NASA TP-2000-209760, March 2000.

[6] Titov, E., and Levin, D., "Extension of the DSMC Method to Higher Pressure Flows," *International Journal of Computational Fluid Dynamics*, Vol. 21, No. 9–10, Oct.–Dec. 2007, pp. 351–368. doi:10.1080/10618560701736221

[7] Rosner, D., and Allendorf, H. D., "High-Temperature Kinetics of Graphite Oxidation by Dissociated Oxygen," *AIAA Journal*, Vol. 3, Aug. 1965, pp. 1522–1523. doi:10.2514/3.3186

[8] Liou, W. W., and Fang, Y., *Microfluid Mechanics Principles and Modeling*, Nanoscience and Technology Series, McGraw–Hill, New York, 2006.

[9] Alexeenko, A., Fedosov, D., Levin, D., Gimelshein, S., and Collins, R., "Performance Analysis of Microthrusters Based on Coupled Thermal-Fluid Modeling and Simulation," *Journal of Propulsion and Power*, Vol. 21, No. 1, 2005, pp. 95–101. doi:10.2514/1.5354

[10] Sun, H., and Faghri, M., "Effect of Surface Roughness on Nitrogen Flow in a Microchannel Using the Direct Simulation Monte Carlo Method," *Numerical Heat Transfer. Part A: Applications*, Vol. 43, No. 1, 2003, pp. 1–8. doi:10.1080/10407780307302

[11] Karniadakis, G., Narayan, A., and Bestok, A., *Microflows and Nanoflows: Fundamentals and Simulation*, Springer2005.

[12] Curry, D., Johansen, K., and Stephens, E., "Reinforced Carbon–Carbon Oxidation Behavior in Convective and Radiative Environments," NASA Technical Paper 1284, 1978.

[13] Bird, G. A., *Molecular Gas Dynamics and the Direct Simulation of Gas Flows*, Clarendon, Oxford, England, U.K., 1994.

[14] Kurotaki, T., "Catalytic Model on SiO_2-Based Surface and Application to Real Trajectory," *Journal of Spacecraft and Rockets*, Vol. 38, No. 5, 2001, pp. 798–800. doi:10.2514/2.3749

[15] Ivanov, M. S., Markelov, G. N., and Gimelshein, S. F., "Statistical Simulation of Reactive Rarefied Flows: Numerical Approach and Application," AIAA Paper 98-2669, June 1998.

[16] *The General Aerodynamic Simulation Program, Computational Flow Analysis Software for the Scientist and Engineer, User's Manual*, Aerosoft Co., Blacksburg, VA, 1996.

[17] Zhong, J., Titov, E., Levin, D., Picetti, D., and Aksamentov, V., "Numerical Simulation of a Micro Flow in and Expanding Channel," AIAA Paper 2006-3597, June 2006.